Journal Pre-proof

NaSn$_2$(PO$_4$)$_3$ submicro-particles for high performance Na/Li mixed-ion battery anodes

Beibei Zhao, Xudong Zhang, Guogang Xu, Kwan San Hui, Jiefang Zhu, Wen He

Please cite this article as: B. Zhao, X. Zhang, G. Xu, K. San Hui, J. Zhu, W. He, NaSn$_2$(PO$_4$)$_3$ submicro-particles for high performance Na/Li mixed-ion battery anodes, *Journal of Alloys and Compounds* (2020), doi: https://doi.org/10.1016/j.jallcom.2020.156082.

This is a PDF file of an article that has undergone enhancements after acceptance, such as the addition of a cover page and metadata, and formatting for readability, but it is not yet the definitive version of record. This version will undergo additional copyediting, typesetting and review before it is published in its final form, but we are providing this version to give early visibility of the article. Please note that, during the production process, errors may be discovered which could affect the content, and all legal disclaimers that apply to the journal pertain.
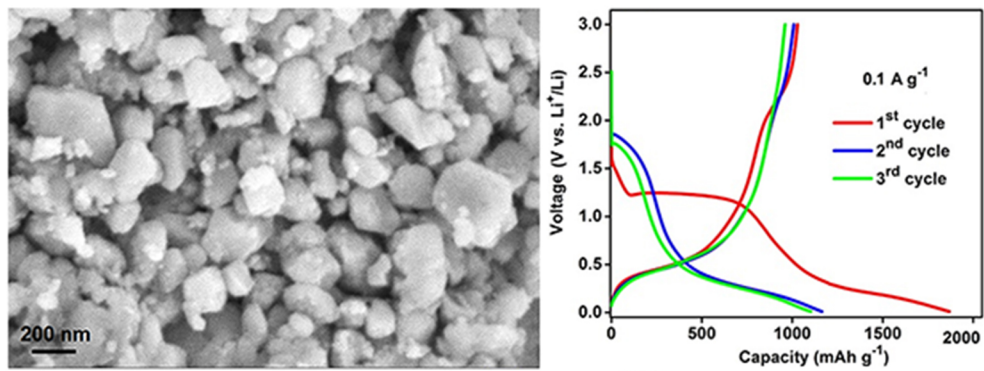
NaSn$_2$(PO$_4$)$_3$ submicro-particles for high performance Na/Li mixed-ion battery anodes

Beibei Zhao [a], Xudong Zhang [a, *], Guogang Xu [b], Kwan San Hui [c], Jiefang Zhu [d] and Wen He [a, *]

[a] *Institute of Materials Science and Engineering, Qilu University of Technology (Shandong Academy of Sciences), Jinan 250353, China.*

[b] *College of Material Science and Engineering, Shandong University of Science and Technology, Qingdao 266590, China*

[c] *Energy and Environment Laboratory, School of Engineering, University of East Anglia (UEA), Norwich, NR4 7TJ, United Kingdom.*

[d] *Department of Chemistry - Ångström Laboratory, Uppsala University, Box 538, SE-75121 Uppsala, Sweden.*

* Corresponding author: Prof. Xudong Zhang, Wen He; Tel: +86 13668813006; +86 18353108836

E-mail address: zxd@qlu.edu.cn (X. Zhang), ORCID ID: https://orcid.org/0000-0002-1384-6545;

hewen1960@126.com (W. He), ORCID ID: https://orcid.org/0000-0001-9665-1075.

Abstract

NaSn$_2$(PO$_4$)$_3$ has open framework, high ionic conductivity, low working potential, high theoretical capacity more than twice of graphite. However, its commercial application is limited by its low electrical conductivity and rapid capacity fading. To overcome this challenge, we synthesize NaSn$_2$(PO$_4$)$_3$ submicro-particles (around 100–300 nm in size) by hydrothermally assisted pyrolysis reactions. The synthsized NaSn$_2$(PO$_4$)$_3$ anode for Na/Li mixed-ion batteries delivers an ultrahigh initial discharge capacities, excellent rate performance and superior cycling stability. This

1   design provides a promising pathway for developing high performance mixed-ion

2   batteries.

3   **Keywords:** Lithium-ion batteries; Ionic conductors; Electrochemistry; Na/Li

4   mixed-ion diffusion

5   ━━━━━━━━━━━━━━━━━━━━━━━━━━━━━━━━━━━

6   Nanoscale domain structure manipulation can dramatically improved energy

7   density and other properties, which may help these materials be more competitive for

8   energy storage applications [1, 2]. To improve the electrochemical performances,

9   nanostructure anode materials have achieved the desired goals, such as to achieve

10 high specific energy, enhance the rate capability and obtain a long cycle life [3-5].

11 Lithium ion batteries (LIBs) with relatively high energy density and long-cycle

12 stability become one of the most promising energy storage systems for electric

13 vehicles and portable electronic devices [6]. However, lithium metal has the low mass

14 fraction (~20 ppm) in the earth's crust, resulting into the continuous increase of LIB

15 cost based on the high demand of Li-based raw materials [7]. And lithium metal has

16 safety issues due to the formation of lithium dendrites [8]. Compared to LIBs,

17 sodium-ion batteries (SIBs) offer multiple advantages such as abundant sodium raw

18 material source, evenly geographical distribution and distinctly lower cost, but there

19 are still many problems for SIBs, such as low reversible capacity, low available

20 energy density and rapid capacity decay [9]. The emergence of Li/Na mixed-ion

21 batteries (LNMIBs) balances the advantageous features of SIBs and LIBs, which

2

1 combine the high energy density of LIBs with the safety and low cost of SIBs [10].

2 Hence, the study of LNMIBs operating at room-temperature has become an important

3 research direction and aroused wide attention [11].

4 In design and fabrication of high-performance LNMIBs, it is highly imperative

5 to develop superior anode materials. Among a large number of anode materials，

6 Sn-based materials are environmental friendliness and low cost. However, some

7 Sn-based materials such as SnO_2, SnS_2, and Sn-based alloys, suffer from enormous

8 volume expansion (≈300%) during the charge-discharge process and intermediate

9 dissolution, resulting in poor cycling stability and capacity retention [20]. In a number

10 of Sn-based materials, Na super ionic conductor (NASICON)-type Sn-based

11 phosphates, such as SnP_2O_7 [12,13], $LiSn_2(PO_4)_3$ [14-16], $NaSn_2(PO_4)_3$ [17-19] etc,

12 have many advantages, such as natural abundance, high ionic conductivity (about 1.5

13 $\times 10^{-5}$ S cm^{-1}), low working potential (less than 0.6 V vs. Li/Li^+), high theoretical

14 capacity (993 mA h g^{-1} for Sn), more than twice of graphite (372 mAh g^{-1}). Compared

15 to Sn-based alloys, $NaSn_2(PO_4)_3$ (NSP) not only owns an open three-dimensional

16 (3D) framework structure, but possesses excellent structural stability and good

17 thermal stability, resulting in smaller volume change during the charge-discharge

18 process. However, the commercial application of NSP is limited by their low

19 electrical conductivity and rapid capacity fading. To improve the electrochemical

20 performances, a variety of nanostructural Sn-based electrodes have achieved the

21 desired goals [20-24]. Especially NSP nano-particles can offer some advantages for

22 Li/Na mixed-ion storage, such as shortening the diffusion length and facilitating the

1 insertion/extraction of mixed-ions, having minimal stress gradient induced by the

2 volume change during the charge/discharge cycles.

3   The attainment of both excellent rate performance and superior cycling stability in

4 anode materials is highly challenging yet critically important in the applications of

5 LNMIBs. As seen from Table S1, although the some publications on various Sn-based

6 phosphate anodes have been reported in the past few years, the results of these

7 publications, such as rate performance and cycling stability, are not pretty. At present,

8 the synthesis methods of Sn-based phosphate negative electrodes mainly include

9 solid-state and sol-gel methods. Although hydrothermal methods for synthesizing

10 electrode materials have been widely studied [25-28], the hydrothermal methods for

11 synthesizing Sn-based phosphate anodes have still not been reported. The results of

12 our test have shown that the hydrothermal process played an important role to control

13 the morphology and crystal structure of electrode materials by controlling the

14 synthesis conditions. Here, we propose a novel Na/Li mixed-ion battery based on NSP

15 anode. The NSP submicro-particles (100-300 nm) (A-NSP) are synthesized by

16 hydrothermally assisted pyrolysis reactions for the first time and the synthesis

17 conditions are optimized. The NSP submicro-particles possess better electrochemical

18 performances than the bare NSP synthesized by sol-gel method (B-NSP), exhibiting

19 significantly enhanced storage capacity and reversibility of Na/Li mixed-ions.

20 Experimental details (material synthesis, characterization and electrochemical

21 evaluation) of NSP samples are reported in Supplementary S1. The challenge of this

22 design is the attainment of both excellent rate performance and superior cycling

1   stability in NSP submicro-particle anode at the same time. The present work is among

2   the best thus far reported for NSP anodes (Table S1). This provides a new strategy for

3   developing   LNMIBs,   highlighting   the   enormous   potential   of $NaSn_2(PO_4)_3$

4   submicro-particle anodes in the applications of LNMIBs.
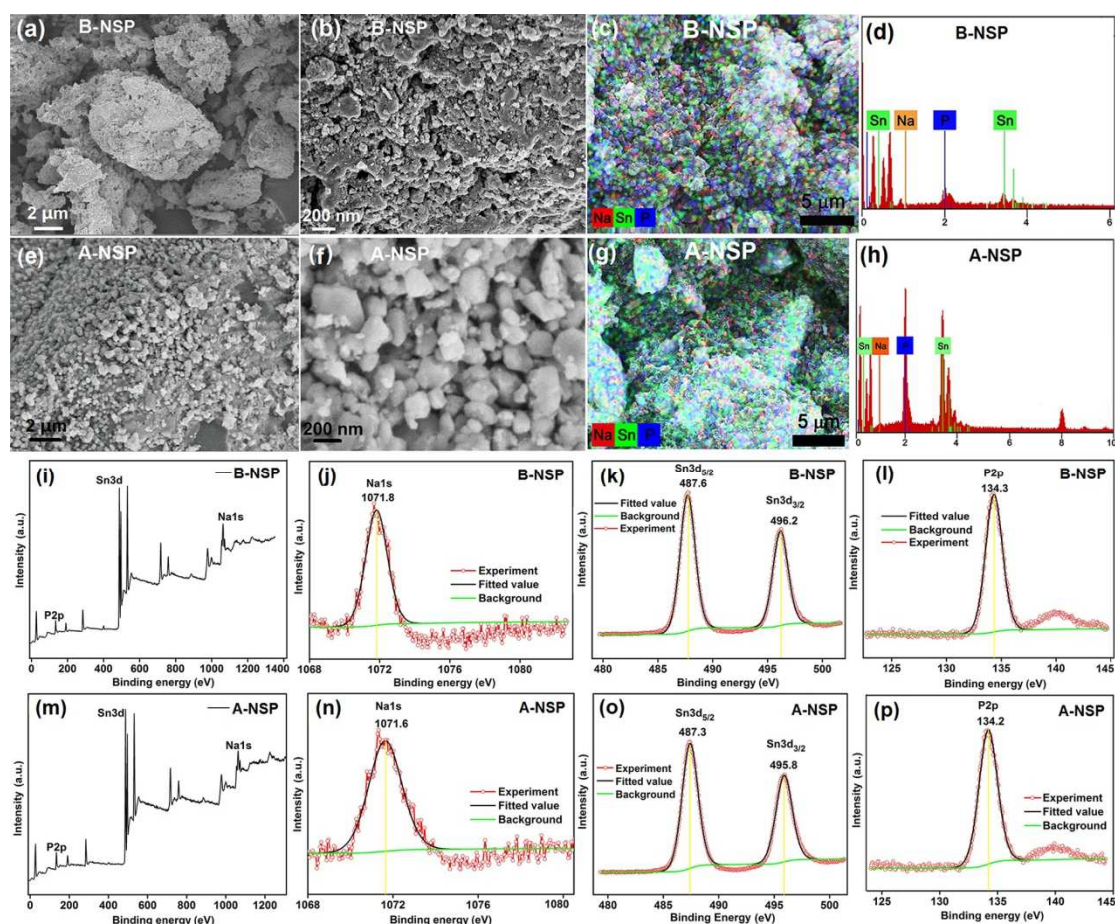
Fig. 1. (ab) SEM images of B-NSP sample synthesized by sol-gel method. (c) SEM–EDS mapping image of Na, Sn and P elements and (d) corresponding spectrum of B-NSP sample. (ef) SEM images of A-NSP sample synthesized by hydrothermally assisted pyrolysis reactions under optimized conditions. (g) SEM–EDS mapping image of element Na, Sn and P and (h) corresponding spectrum of A-NSP sample. (i) XPS survey spectrum of B-NSP sample and high resolution XPS spectra of Na1s (j), Sn 3d (k) and P 2p (l). (m) XPS survey spectrum of A-NSP sample and high resolution XPS spectra of Na1s (n), Sn 3d (o) and P 2p (p).

15   The morphology, elemental composition and fine microstructure of the

16   as-prepared   samples   were   investigated   by   field   emission   scanning   electron

1   microscopy (FE-SEM), X-ray energy dispersive spectrometry (EDS) and

2   high-resolution transmission electron microscopy (HRTEM), respectively. The SEM

3   images in Fig. 1ab show that the B-NSP sample synthesized by the sol-gel method

4   consists of many irregular agglomeration particles and these hard agglomerations are

5   formed by the accumulation of many thin slices (Fig. 1b). The elemental mapping

6   image (Fig. 1c) and corresponding spectrum (Fig. 1d) of the B-NSP sample confirm

7   the existence and distribution of Na, Sn and P elements. Fig. 1e and Fig. 1f are the

8   SEM images of the A-NSP sample synthesized by the hydrothermally assisted

9   pyrolysis reactions. It can be seen that the A-NSP sample contains submicro-particles

10   (around 100–300 nm in size) without hard aggregate (Fig. 1f). The elemental mapping

11   image (Fig. 1g) and corresponding spectrum (Fig. 1h) of the A-NSP sample verify the

12   homogeneous distribution of Na, Sn and P elements. In order to further prove the

13   existence of elements and their chemical states, the X-ray photoelectron spectroscopy

14   (XPS) was carried out. As shown in Fig. 1i and Fig. 1m, Na, Sn and P are discovered

15   in the survey spectra of both B-NSP and A-NSP samples, which is consistent with the

16   elemental constitute of $NaSn_2(PO_4)_3$. The High-resolution XPS spectra of Na1s (Fig.

17   1j), Sn 3d (Fig. 1k) and P 2p (Fig. 1l) correspond to Na^+, Sn^{4+} and P^{5+}, respectively

18   [21,29], confirming the elemental chemical states of B-NSP. Compared the

19   high-resolution XPS spectra of B-NSP and A-NSP samples, all peak positions of

20   A-NSP sample shifted slightly toward lower binding energy, suggesting that the

21   A-NSP has the higher electrochemical activity than B-NSP. These submicro-particles

22   can shorten the pathway lengths of the ion diffusion effectively during the Li^+/Na^+

1   insertion/extraction processes [30].
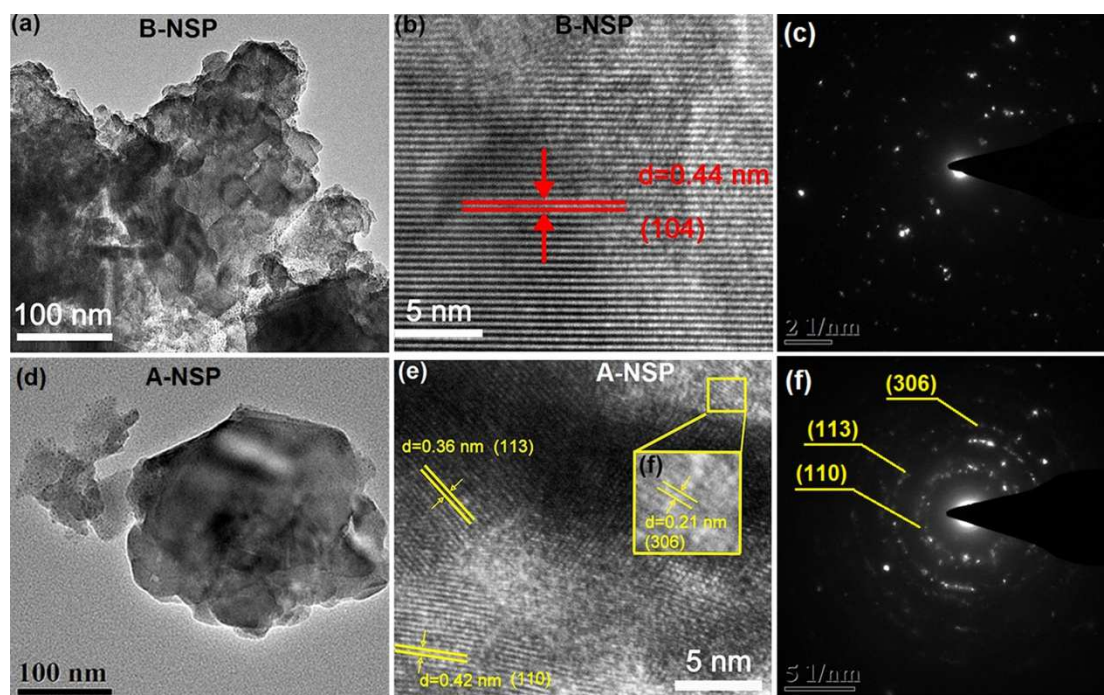
2

3   **Fig. 2.** TEM image (a), HRTEM image (b) and corresponding selected area electron
4   diffraction (SAED) pattern (c) of B-NSP sample. TEM image (d), HRTEM image (e)
5   and corresponding SAED pattern (f) of A-NSP sample.
6

7   Fig. 2a is TEM image of a thin slice particle in B-NSP sample, which consists of

8   hard agglomerated nanoparticles. Its HRTEM image clearly reveals lattice fringes of

9   0.44 nm, corresponding to the (104) plane of B-NSP sample (Fig. 2b). The selected

10   area electron diffraction (SAED) pattern shows irregular diffraction spots of hard

11   agglomeration particle (Fig. 2c). The TEM image of A-NSP sample shows that a

12   single dispersed submicro-particle has relatively regular grain shape, denser structure

13   and smoother surface (Fig. 2d). As revealed by the HRTEM image, lattice fringes of

14   0.42, 0.36 and 0.21 nm are clearly observed, which correspond to the (110), (113) and

15   (306) planes of A-NSP sample (Fig. 2e). Combined with the SAED pattern (Fig. 2f),

16   all these diffraction rings confirmed the successful preparation of A-NSP

17   submicro-particles.
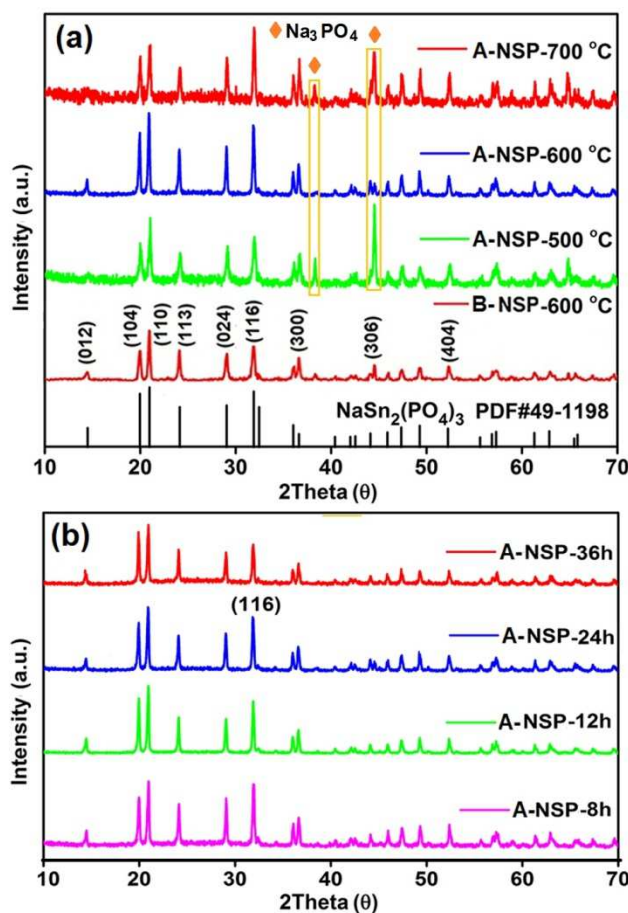
1

Fig. 3. XRD patterns of A-NSP synthesized by hydrothermally assisted pyrolysis reactions and B-NSP samples synthesized by sol-gel method. (a) The samples synthesized by hydrothermal reaction for 24 h and then with different heat treatment temperatures for 8 h under N_2 atmosphere. (b) The samples synthesized with different hydrothermal reaction times at 180 °C and then at 600 °C for 8 h under N_2 atmosphere.

The X-ray diffraction (XRD) patterns of the samples synthesized at different heat treatment temperatures (Fig. 3a) and with different hydrothermal reaction time at 180 °C (Fig. 3b) reveal their crystallographic phase and crystallinity, respectively. It is clear that the sharp and intense peaks of all samples agree well with the standard card (PDF# 49-1198) of $NaSn_2(PO_4)_3$, which indicate that all the samples have well crystallized characteristic of R-3C space group of rhombohedral lattice with a=b= 8.507 Å and c= 22.467 Å [17]. The A-NSP sample synthesized by hydrothermal

8

1   reaction for 24 h and then at 600 °C for 8 h has no peaks of any mixed phase, while

2   the A-NSP sample synthesized at 700 and 500 °C contains the diffraction peaks of

3   Na_3PO_4 impurity phase (PDF# 30-1232) (Fig. 3a). Supplementary Tables S2-S4

4   present the summary of the lattice parameters of the different samples synthesized

5   with different conditions calculated by using Jade 6 XRD pattern-processing software,

6   respectively. The results show that the crystallinity of A-NSP-24h sample synthesized

7   by hydrothermally assisted pyrolysis reactions is higher than that of B-NSP

8   synthesized by sol-gel method, and the strain (0.192%) of A-NSP sample is obviously

9   smaller than that (0.375%) of B-NSP (see Table S2). Although the A-NSP-12h sample

10 shows the smallest strain, it has lower crystallinity and smaller crystallite size

11 compared with A-NSP-24h sample. So the A-NSP submicro-particles have good

12 structural stability, which has benefits for enhancing electrochemical cycling stability,

13 showing the best electrochemical performances compared with other samples [30].

14   First, optimization studies are carried out for A-NSP submicro-particle anodes

15 synthesized by hydrothermally assisted pyrolysis reactions under the different

16 preparation conditions by using the galvanostatic charge-discharge test. The

17 electrochemical properties were evaluated in the half cells assembled with the

18 different anodes and Li metal cathode. Fig. 4 shows the charge-discharge curves of

19 the A-NSP anodes synthesized under the different preparation conditions. Fig. S3

20 shows the rate performances of the A-NSP anodes synthesized under the different

21 preparation conditions. The results show that both the heat treatment temperature and

22 the heat treatment time have a great impact on electrochemical performances than
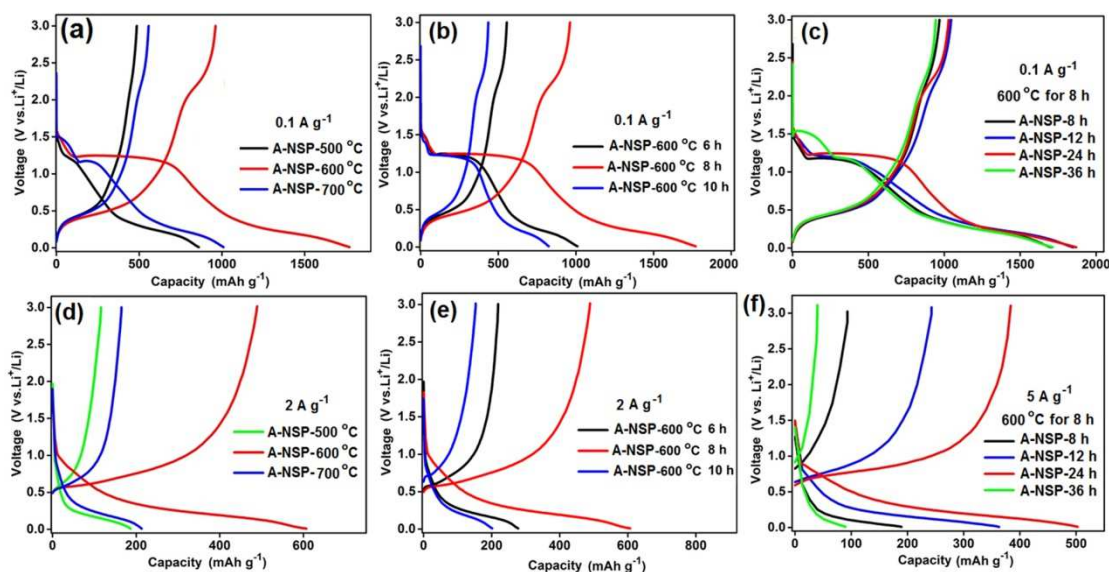
Fig. 4. Charge-discharge curves of the A-NSP anodes synthesized under the different preparation conditions at 0.1 and 2 A g^{-1}. (a and d) Hydrothermal treatment at 180 ^{o}C for 24 h and then heat treatment at different temperatures for 8 h. (b and e) Hydrothermal treatment at 180 ^{o}C for 24 h and then heat treatment at 600 ^{o}C for different heat treatment time. (c and f) Hydrothermal treatment at 180 ^{o}C for different hydrothermal treatment time and then heat treatment at 600 ^{o}C for 8 h.

hydrothermal reaction time. Fig. 4c shows that the heat reaction time has a small impact on the initial discharge/charge specific capacity and the plateau at 1.25 V. However, the hydrothermal treatment time also plays an important role in forming submicro-particles and improving the high rate performance (Fig. 4f). The A-NSP anode synthesized by hydrothermal treatment at 180 °C for 24 h and then by heat treatment at 600 °C for 8 h has the highest discharge/charge capacities and the best rate performances. This is because it has small strain, appropriate crystallization degree and crystalline size (Table S3 and S4). Fig. S4 shows the electrochemical performances of the B-NSP anodes synthesized at the different heat treatment temperatures. The results show that the B-NSP anode synthesized at 600 °C for 8 h has the best rate performances (Fig. S4b).

10

1   The A-NSP anode synthesized under the optimized conditions exhibits a ultrahigh

2   initial discharge/charge specific capacity of 1868.5/1028.9 mAh g^{-1} at a current

3   density of 0.1 A g^{-1} (Fig. 5a), which are much higher than that (857.5/466.3 mAh g^{-1})

4   of B-NSP anode synthesized by sol-gel method under same conditions (Fig. S4b). The

5   theoretical capacity of the first discharge of $NaSn_2(PO_4)_3$ is about 826 mAh g^{-1}

6   according to the literature [18]. The initial discharge specific capacity of the A-NSP

7   anode is 1868.5 mAh g^{-1} at 0.1 A g^{-1}, exceeding the theoretical capacity by 1042.5

8   mAh g^{-1}. The exceeding capacity can be ascribed to the formation of SEI layer on the

9   surface of electrode [18]. Its discharge/charge capacities still remain at 502.6/383.6

10   mAh g^{-1} even at a higher current density of 5 A g^{-1} (Fig. 5b), and the B-NSP anode

11   only has the discharge/charge capacities of 218.0/141.1 mAh g^{-1} at 5 A g^{-1} (Fig. S4b).

12   The compare results show that the A-NSP anode also has the superior rate capability

13   than that of B-NSP anode. When the current density is from 0.1 to 5Ag^{-1}, the

14   discharge capacity of A-NSP anode is from 1868.5 to 502.6 mAh g^{-1} (Fig. 5b).

15   However, the rate performance of B-NSP anode is very poor and only has the

16   discharge capacity of 218 mAh g^{-1} at 5 A g^{-1} (Fig. S4b). Fig. S5 shows the

17   electrochemical performance comparison of the half cells assembled with the different

18   anodes. The result shows that the A-NSP anode delivers much better long cycling

19   performance than the B-NSP anode (Fig. S5e).

20   Fig. 5a also shows that the A-NSP anode has a clear plateau at approximately

21   1.25 V in the first discharge process, which results in irreversible capacity of 35.8%

22   and low initial Coulumbic efficiency. The discharge capacity (about 625 mAh g^{-1}) of
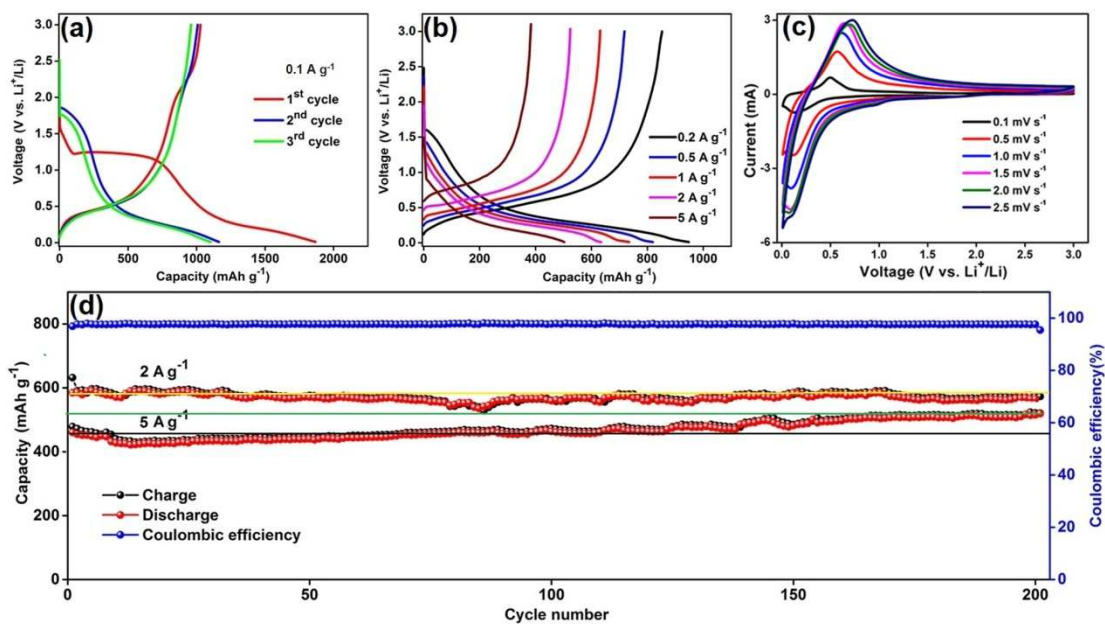
11

Fig. 5. Electrochemical performances of the A-NSP anode synthesized under optimum conditions. (a) The charge-discharge curves for the first three cycles at 0.1 A g^{-1}. (b) The charge-discharge curves at different current densities from 0.2 Ag^{-1} to 5Ag^{-1}. (c) The CV curves at various sweep rates in the voltage range of 0.0–3.0 V. (d) Long cycling performance comparison at different current densities.

this plateau corresponds to some parasitic surface reactions, such as the formation of

Li salt inactive matrix and the irreversible decomposition of electrolyte [14]. This

plateau seems to be influenced by synthesis conditions (Fig. 4a-c), and the A-NSP

anode synthesized under optimum conditions has a longest plateau at 1.25 V. After

this plateau, the sloping plateau from 1.0 V to 5 mV with the discharge capacity of

1068 mAh g^{-1} correlates to the reversible alloying reaction accompanying Li/Na

mixed-ion insertion into Sn and the formation of SEI layer on the surface of electrode

[18]. The charge/discharge profiles overlap after the first cycle indicating good

reversibility and Coulumbic efficiency. The corresponding charge-discharge curves at

different current densities show that their charge-discharge plateau (about at 0.5 V)

increases slightly with the increasing charge-discharge current densities (Fig. 5b),

1   indicating that the A-NSP anode has fast kinetics property and weak electrochemical

2   polarization [32]. To further confirm the electrochemical reaction of A-NSP anode,

3   the cyclic voltammogram (CV) measurements were carried out in the voltage range of

4   0.0–3.0 V (Fig. 5c). In the CV curve at a scan rate of 0.1 mV s^{-1}, a voltage plateau

5   appears at 0.22 V in the discharge process and a voltage plateau appears at 0.54 V in

6   the charge process correspond to the alloying and dealloing process [14]. With an

7   increasing scan rate, the CV curves of A-NSP anode basically keep the shape and

8   contour, indicating the high reversibility and weak polarization of the electrochemical

9   reaction in the battery. The excellent long cycling stability and high Coulombic

10   efficiency of A-NSP anode were verified at the higher current densities of 2 and 5 A

11   g^{-1} for 200 cycle (Fig. 5d), which are much higher than previous reported results

12   [12-19]. It is interesting that, when the A-NSP anode was cycled at the higher current

13   density of 5 A g^{-1}, its capacity displays a good cyclability for the first 100 cycles, and

14   very little change, but continuously increases after 100 cycles. After 200 cycles at 5 A

15   g^{-1}, the reversible capacity still reaches 465 mAh g^{-1}, corresponding to capacity

16   retention of 106% and Coulombic efficiency of 99% for the first cycle. This may be

17   because the electrochemical active sites on the surface of the submicro-particles are

18   more easily activated at high current density [33] (Fig. 6f). Moreover, the nanosized

19   Na substituted Li_3PO_4 ($Li_{3-x}Na_xPO_4$) material with high ionic conductivity (6.5×10^{-5} S

20   cm^{-1}) was more easily formed in-situ on the surface of the submicro-particles,

21   providing a better matrix and more electrochemical active sites. Therefore, these

22   reasons lead to that the capacity retention is higher than 100% in Fig. 5d.

1   The SEM images of A-NSP and B-NSP anodes at the higher current densities of

2   2 A g^{-1} after 50 cycles are shown in Fig. S6. The results show that A-NSP anode has

3   more compact and uniform microstructure (Fig. S6d) and nanostructure (Fig. S6f)

4   than B-NSP anode (Fig. S6a-c). It also further confirms that the A-NSP anode has

5   better structural stability during the cycle. There are two main reasons: (1) in the

6   preparation process of anode, the A-NSP submicro-particles with different size

7   (100–300 nm) without hard aggregate can tightly pack together; (2) the A-NSP

8   submicro-particles possess higher crystallinity and smaller strain than B-NSP (see

9   Table S2). So the A-NSP anode shows better rate performance and cycling stability

10   than B-NSP.

11
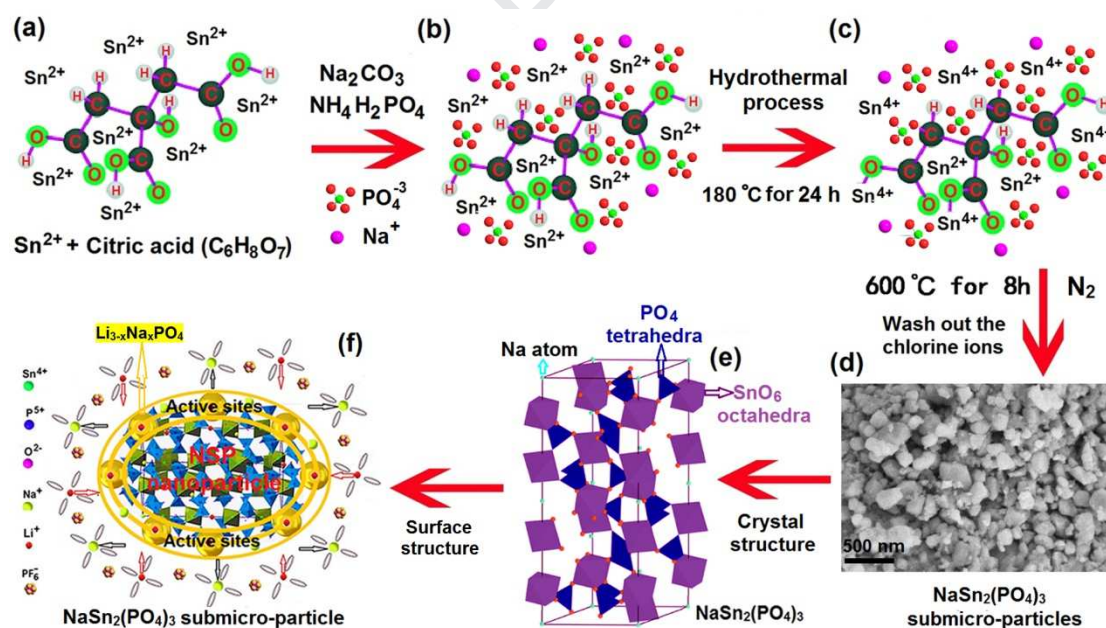
12 **Fig. 6.** (a-d) Synthetic mechanism diagrams of A-NSP submicro-particles. (e) Crystal
13 structure of NSP. (f) Surface structure of A- NSP submicro-particle.
14

15   The synthetic mechanism of A-NSP submicro-particles is proposed as shown in

16   Fig. 6a-d. In the synthesis, Sn ion solution, Na$_2$CO$_3$ and NH$_4$H$_2$PO$_4$ were mixed to

17   form the mixture solution of precursor (Fig. 6ab). In the hydrothermal treatment

14

1   process, Sn^{2+} ions are oxidized to Sn^{4+} ions, leading to the formation of precursor

2   particles (Fig. 6c). After the heat treatment the A-NSP submicro-particles were

3   obtained (Fig. 6d). The crystal structure of $NaSn_2(PO_4)_3$ is shown in Fig. 6e. This

4   structure consists of a three-dimensional framework of corner-sharing slightly

5   distorted SnO_6 octahedra and PO_4 tetrahedra [19]. Fig. 6 e shows the surface structure

6   of A-NSP submicro-particle. The insertion/extraction reactions of Na/Li mixed ions in

7   the processes of charging and discharging can be presented as below equations:

8   $$Na_{1-x}Li_xSn_2\,(PO_4)_3 + (8-x)Li^+ + xNa^+8e^- \rightarrow 3Li_{3-x}Na_xPO_4 + 2Sn \qquad (1)$$

$$5Sn + (22-x)Li^+ + xNa^+ + 22e^- \leftrightarrow Li_{22-x}Na_xSn_5 \qquad (2)$$
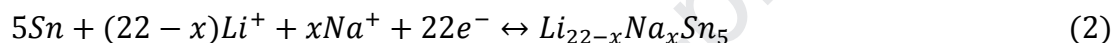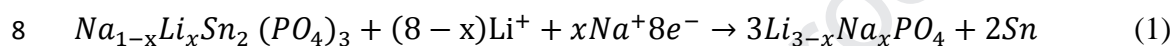
9   Our previous results have prove the Na/Li mixed-ion electrolyte and the active

10 $Li_{3-x}Na_xPO_4$ with high ionic conductivity are formed by ion exchange during the

11 charge/discharge process [34,35]. Moreover, the size effect of A-NSP

12 submicro-particles can greatly enhance the transports of Li^+/Na^+ mixed-ions and

13 electrons to keep the charge balance and relieve the strain caused by the volumetric

14 change [36].

15   In summary, the A-NSP submicro-particle anode synthesized by hydrothermally

16 assisted pyrolysis reactions has better electrochemical performances than the B-NSP

17 anode synthesized by sol-gel method. The A-NSP submicro-particle anode for

18 LNMIBs not only exhibits an ultrahigh initial discharge capacities and excellent rate

19 performance, but also shows superior cycling stability and high Coulombic efficiency.

20 This structure design provides a promising pathway for developing high performance

21 Na/Li mixed-ion battery anodes.

References

[1] S. Zhang, J. Chen, T. Tang, Y. Jiang, G. Chen, Q. Shao, C. Yan, T. Zhu, M. Gao, Y.Liu, H. Pan, J. Mater. Chem. A 6 (2018) 3610–3624.

[2] S. Zhang, T. Tang, Z. Ma, H. Gu, W. Du, M. Gao, Y. Liu, D. Jian, H. Pan, J. Power Sources 380 (2018) 1–11.

[3] Y. Hu, X. Zhu, L. Wang, ChemSusChem 136 (2020) 1366-1378.

[4] A. A.Voskanyan, C.-K. Ho, K.Y. Chan, J. Power Sources 421 (2019) 162–168.

[5] K.O. Ogunniran, G. Murugadoss, R. Thangamuthu, S.T. Nishanthi, J Alloy. Compd. 786 (2019) 873–883.

[6] Z. Liu, Q. Yu, Y. Zhao, R. He, M. Xu, S. Feng, S. Li, L. Zhou, L. Mai, Chem. Soc. Rev. 48 (2019) 285–309.

[7]. W. Kang, Y. Wang, J. Xu, J. Mater. Chem. A 5 (17) (2017) 7667–7690.

[8] K. Zhang, X. Zhang, W. He, W. Xu, G. Xu, X. Yi, X. Yang, J. Zhu, J. Mater. Chem. A 7 (2019) 9890–9902.

[9] X. Dou, I. Hasa, D. Saurel, C. Vaalma, L. Wu, D. Buchholz, D. Bresser, S. Komaba, S. Passerini, Materialstoday 23 (2019) 87–104.

[10] X. Zhang, Z. Bi, G. Xu, C. Li, W. He, J. Zhu, J. Power Sources 438 (2019) 226980.

[11] X. Zhang, X. Xu, Y. Hu, G. Xu, W. He, J. Zhu, NPG Asia Mater. 12 (2020) 1–11.

[12]. J. Pan, S. Chen, D. Zhang, X. Xu, Y. Sun, F. Tian, P. Gao, J. Yang, Adv. Funct. Mater. 28 (2018) 1804672.

[13]. I. Bezza, V. Trouillet, A. Fiedler, M. Bruns, S. Indris, H. Ehrenberg, I. Saadoune, Electrochimica Acta 252 (2017) 446–452.

[14]. J. Tian, D. Wang, Z. Shan, J. Power Sources 361 (2017) 96–104.

[15]. W.-J. Cui, J. Yi, L. Chen, C.-X. Wang, Y.-Y Xia, J. Power Sources 217 (2012) 77–84.

[16] N. Bounar, A. Benabbas, P. Ropa, J.-C. Carru, Advances in Materials and Processing Technologies 3 (2017) 241–249.

[17] B. Liu, Y. Xing, X. Sun, L. Liu, S.Y. Hou, Mater. Lett. 63 (2009) 2548–2551.

[18] P. Hu, J. Ma, T. Wang, B. Qin, C. Zhang, C. Shang, J. Zhao and G. Cui, Chem. Mater. 27 (2015) 6668–6674.

[19] S. Difi, A. Nassiri, I. Saadoune, M. T. Sougrati, P.-E.Lippens, The Journal of Physical Chemistry C 122 (2018) 11194–11203.

[20]. B. Huang, X. Li, Y. Pei, S. Li, X. Cao, R.C. Massé, G. Cao, Small 12 (2016) 1945–1955.

[21]. S. Abouali, M.A. Garakani, J.K. Kim, Electrochimica Acta. 284 (2018) 436–443.

[22]. P. Xue, N. Wang, Y. Wang, Y. Zhang, Y. Liu, B. Tang, Z. Bai, S.Dou, Carbon. 134 (2018)

222–231.

[23]. Y. Zhang, C. Zhao, Z. Zeng, J.M. Ang, B. Che, Z. Wang, X. Lu, Electrochimica Acta. 278 (2018) 156–164.

[24]. S. Tao, D. Wu, S. Chen, B. Qian, W. Chu, L.Song, Chem. Commun. 54 (2018) 8379–8382.

[25] S. Yuvaraj, K. Karthikeyan, L. Vasylechko, R. KalaiSelvan, Electrochimica Acta 158 (2015)

446–456.

[26] K. VijayaSankar, S. S. SubramaniSurendran, S. ChanJun, R. KalaiSelvan, J. Colloid Interf.

Sci. 513 (2018) 480–488.

[27] K. Balakrishnan , V. Mignesh, A. Subramania, RSC Advances 7 (2017) 5853–5862.

[28] E. N. Gorenskaia, B. Ch. Kholkhoev, V. G. Makotchenko, M. N. Ivanova, V. E. Fedorov,. V. F.

Burdukovskii, J. Nanosci Nanotechno. 20 (2020) 3258–3264 (7).

[29] Y. Zhang, P. Zhu, L. Huang, J. Xie, S. Zhang, G. Cao, X. Zhao, Adv. Funct. Mater. 25 (3) (2014) 481–489.

[30] G. Han, J.H. Um, H. Park, K. Hong, W.-S. Yoon, H. Choe, Scripta Materialia 163 (2019) 9–13.

[31] B. W. Byles, M. Clites, D. A. Cullen, K. L. More, E. Pomerantseva, Ionics 25 (2019) 493–502.

[32] J. Liang, Y. Lu, J. Wang, X. Liu, K. Chen, W. Ji, Y. Zhu, D. Wang, J. Energy Chem. 47 (2020) 188–195.

[33] L. Kong, M. Zhong, W. Shuang, Y. Xu, X.-H. Bu, Chem. Soc. Rev. (2020) https://doi.org/10.1039/C9CS00880B.…

[34] X. Zhang, X. Xu, W. He, G. Yang, J. Shen, J. Liu, Q, Liu J. Mater. Chem. A 3 (2015)

22247–22257.

[35] W. He, X. Zhang, C. Jin, Y. Wang, S. Mossin, Y. Yue, J. Power Sources 342 (2017) 717–725.

[36] Y. Wang, S. Luo, M. Chen, L. Wu, Adv. Funct. Mater. 30 (2020) 2000373, https://doi.org/10.1002/adfm.202000373.

17

1

Fig. 1. (ab) SEM images of B-NSP sample synthesized by sol-gel method. (c) SEM–EDS mapping image of Na, Sn and P elements and (d) corresponding spectrum of B-NSP sample. (ef) SEM images of A-NSP sample synthesized by hydrothermally assisted pyrolysis reactions under optimized conditions. (g) SEM–EDS mapping image of element Na, Sn and P and (h) corresponding spectrum of A-NSP sample. (i) XPS survey spectrum of B-NSP sample and high resolution XPS spectra of Na1s (j), Sn 3d (k) and P 2p (l). (m) XPS survey spectrum of A-NSP sample and high resolution XPS spectra of Na1s (n), Sn 3d (o) and P 2p (p).

Fig. 2. TEM image (a), HRTEM image (b) and corresponding selected area electron diffraction (SAED) pattern (c) of B-NSP sample. TEM image (d), HRTEM image (e) and corresponding SAED pattern (f) of A-NSP sample.

Fig. 3. XRD patterns of A-NSP synthesized by hydrothermally assisted pyrolysis reactions and B-NSP samples synthesized by sol-gel method. (a) The samples synthesized by hydrothermal reaction for 24 h and then with different heat treatment temperatures for 8 h under N_2 atmosphere. (b) The samples synthesized with different hydrothermal reaction times at 180 °C and then at 600 °C for 8 h under N_2 atmosphere.

Fig. 4. Charge-discharge curves of the A-NSP anodes synthesized under the different preparation conditions at 0.1 and 2 A g^{-1}. (a and d) Hydrothermal treatment at 180 °C for 24 h and then heat treatment at different temperatures for 8 h. (b and e) Hydrothermal treatment at 180 °C for 24 h and then heat treatment at 600 °C for different heat treatment time. (c and f) Hydrothermal treatment at 180 °C for different hydrothermal treatment time and then heat treatment at 600 °C for 8 h.

Fig. 5. Electrochemical performances of the A-NSP anode synthesized under optimum conditions. (a) The charge-discharge curves for the first three cycles at 0.1 A g^{-1}. (b) The charge-discharge curves at different current densities from 0.2 Ag^{-1} to 5Ag^{-1}. (c) The CV curves at various sweep rates in the voltage range of 0.0–3.0 V. (d) Long cycling performance comparison at different current densities.

Fig. 6. (a-d) Synthetic mechanism diagrams of A-NSP submicro-particles. (e) Crystal structure of NSP. (f) Surface structure of A- NSP submicro-particle.

Declaration of interests

v☐v The authors declare that they have no known competing financial interests or personal relationships that could have appeared to influence the work reported in this paper.

☐The authors declare the following financial interests/personal relationships which may be considered as potential competing interests: